Single-molecule analysis reveals the phosphorylation of FLS2 regulates its spatiotemporal dynamics and immunity

Yaning Cui[1,2,5], Hongping Qian[2,5], Jinhuan Yin[2], Changwen Xu[2], Pengyun Luo[2], Xi Zhang[2], Meng Yu[3], Bodan Su[4], Xiaojuan Li[2], Jinxing Lin[1,2*]

[1]State Key Laboratory of Tree Genetics and Breeding, College of Biological Sciences and Technology, Beijing Forestry University, Beijing 100083, China;
[2]National Engineering Research Center of Tree Breeding and Ecological Restoration, College of Biological Sciences and Technology, Beijing Forestry University, Beijing 100083, China
[3] College of Life Sciences, Hebei Agricultural University, Baoding, 071001, China
[4] Biotechnology Research Institute, Beijing 100081, China
[5] These authors contributed equally
[*]Correspondence: Jinxing Lin (linjx@ibcas.ac.cn)

Summary

Phosphorylation of receptor kinase (RK) is pivotal for signaling in pattern-triggered immunity (PTI). The *Arabidopsis thaliana* FLAGELLIN-SENSITIVE2 (FLS2) is a conserved 22 amino acid sequence in the N-terminal region of flagellin (flg22), initiating plant defense pathways. However, the dynamic FLS2 phosphorylation regulation at the plasma membrane in response to flg22 needs further elucidation. Through single-particle tracking, we demonstrated that the Ser-938 phosphorylation site influences flg22-induced FLS2 spatiotemporal dynamics and dwell time. Förster resonance energy transfer-fluorescence lifetime (FRET-FLIM) imaging microscopy, coupled with protein proximity indexes (PPI), revealed increased co-localization of FLS2/FLS2^{S938D}-GFP with *At*Rem1.3-mCherry in response to flg22. In contrast, FLS2^{S938A}-GFP shows no significant changes, indicating that Ser-938 phosphorylation influences the efficient FLS2 sorting into *At*Rem1.3-associated microdomains. Significantly, Ser-938 phosphorylation enhanced flg22-induced internalization and immune responses, thus

demonstrating its regulatory role in FLS2 partitioning into functional *At*Rem1.3-associated microdomains for activating flg22-induced plant immunity.

Key words: single-molecule analysis; phosphorylation; spatiotemporal dynamics; *At*Rem1.3-associated microdomains; endocytosis; immunity;

Introduction

Receptor kinase (RK) are structurally conserved proteins, featuring an extracellular domain, a single transmembrane region, and a cytoplasmic kinase domain. The cytoplasmic kinase domain consists of a protein kinase catalytic domain (PKC) and a juxtamembrane region, containing crucial phosphorylation sites on specific Ser and/or Thr residues essential for pattern-triggered immunity (PTI), the initial defense layer in plants (Mitra et al., 2015; Gada et al., 2022). PTI efficiently inhibits pathogen infection by activating defense responses, exemplified by the FLS2 signaling pathway (Li et al., 2016a; Zhai et al., 2021; Yu et al., 2023). Upon recognizing flg22, FLS2 interacts with the co-receptor Brassinosteroid-Insensitive 1-associated Kinase 1 (BAK1), initiating phosphorylation events through the activation of receptor-like cytoplasmic kinases (RLCKs) such as BOTRYTIS-INDUCED KINASE 1 (BIK1) to elicit downstream immune responses (Chinchilla et al., 2006; Li et al., 2016b; Majhi et al., 2021).

Protein phosphorylation, a vital posttranslational modification, plays a well-established and significant role. Research suggests that alterations in protein phosphorylation affect protein dynamics and subcellular trafficking (Palladino et al., 2022; Kontaxi et al., 2023). In plants, phosphorylation of proteins can coalesce into membrane microdomains, forming platforms for active protein function at the plasma membrane (PM) (Bücherl et al., 2017). For example, Xue et al. (2018) demonstrated that phosphorylation of the blue light receptor phot1 accelerates PM movement, enhancing interaction with

*At*Rem1.3-mCherry, a sterol-rich lipid marker. This underscores protein phosphorylation's crucial role in PM dynamics and membrane partitioning. Upon flg22 treatment, multiple FLS2 phosphorylation sites activate, with FLS2 Serine-938 phosphorylation playing a pivotal role in defense activation (Cao et al., 2013). While FLS2 Ser-938 is crucial for plant PTI, its impact on immunity through spatiotemporal dynamics remains unknown.

Membrane microdomains, dynamic structures rich in sterols and sphingolipids, are crucial in regulating plasma membrane (PM) protein behavior (Boutté et al., 2020). Specific proteins like Flotillins and Remorins can uniquely label these microdomains within living cells (Cui et al., 2018; Bücherl et al., 2017). Various stimuli can induce PM proteins to move into mobile or immobile microdomains, suggesting a connection between microdomains and signal transduction (Kim et al., 2018). For instance, Xing et al. (2022) demonstrated that sterol depletion significantly impacts the dynamics of flg22-activated FER–GFP, emphasizing microdomains' role in the lateral mobility and dissociation of FER from the PM under flg22 treatment. However, the spatial coordination of FLS2 dynamics and signaling at the PM, along with their relationships with microdomains, remains poorly understood.

To investigate if FLS2 Ser-938 phosphorylation-mediated immune response is linked to its microdomain, we analyzed diffusion and dwell time of FLS2 phospho-dead and phospho-mimic mutants at the PM before and after flg22 treatments. Our results show that flg22-induced dynamic and dwell time changes are abolished in $FLS2^{S938A}$. Using FLIM-FRET and smPPI techniques, we discovered that FLS2 in different phosphorylation states exhibited distinct membrane microdomain distribution and endocytosis. Additionally, various phenotypic experiments demonstrated that the immune response of phosphorylated $FLS2^{S938D}$ was similar to wild-type FLS2, while weakened in transgenic plants with dephosphorylated $FLS2^{S938A}$. These findings contribute to the theoretical foundation for studying plant immunity

regulation through phosphorylation.

Results and Discussion

The Ser-938 phosphorylation site changed the spatiotemporal dynamics of flg22-induced FLS2 at the plasma membrane

Previous studies highlight the crucial role of membrane protein phosphorylation in fundamental cellular processes, including PM dynamics (Vitrac et al., 2019; Offringa et al., 2013). *In vitro* mass spectrometry (MS) identified multiple phosphorylation sites in FLS2. Genetic analysis further identified Ser-938 as a functionally important site for FLS2 *in vivo* (Cao et al., 2013). FLS2 Ser-938 mutations impact flg22-induced signaling, while BAK1 binding remains unaffected, thereby suggesting Ser-938 regulates other aspects of FLS2 activity (Cao et al., 2013). To unravel the immune response regulation mechanisms via FLS2 phosphorylation, we generated transgenic Arabidopsis plants expressing C-terminal GFP-fused FLS2, S938A, or S938D under the FLS2 native promoter in the *fls2* mutant background (Figure S1A). Using VA-TIRFM with single-particle tracking (Figure 1A and 1B), we investigated the diffusion dynamics of FLS2 phospho-dead and phospho-mimic mutants, following previous reports (Geng et al., 2022). Upon flg22 treatment, FLS2^{S938D}-GFP spots exhibited longer motion trajectories, while FLS2^{S938A}-GFP spots were limited to shorter motion tracks (Figure 1C). The results indicate significant changes in the diffusion coefficients and motion ranges of FLS2/FLS2^{S938D}-GFP after flg22 treatment, whereas FLS2^{S938A}-GFP showed no significant differences (Figure 1D and 1E). Similar outcomes were observed using Uniform Manifold Approximation and Projection (UMAP) technology (Dorrity et al., 2020) and fluorescence recovery after photobleaching (FRAP) (Greig et al., 2021) (Figure 1F, 1G and S1B, F), supporting the essential role of the S938 phosphorylation site in flg22-induced lateral diffusion of FLS2 at the PM.

Using VA-TIRFM, we analyzed FLS2 particle dwell time across various phosphorylation states. The results revealed that flg22 treatment significantly reduced the fluorescence trajectory of FLS2 molecules compared to the control (Figure 1H and S1C), indicating that Ser-938 phosphorylation influences flg22-induced dwell times of FLS2 at the PM. Subsequently, real-time dynamic analysis through the Kymograph technique provided spatiotemporal information via frame-by-frame tracking (Zhou et al., 2020). Compared to FLS2-GFP and FLS2^{S938D}-GFP, FLS2^{S938A}-GFP showed nearly linear fluctuations in fluorescence intensity under flg22 conditions, and the duration of fluorescence retention was essentially unchanged (Figure S1D). To further confirm this, we quantified FLS2 dwell times using exponential function fitting (Figure 1I and S1E). After flg22 treatment, FLS2^{S938D}-GFP dwell times significantly decreased, resembling those of FLS2-GFP. Although the FLS2^{S938A}-GFP plants, dwell times appeared to slightly decrease with flg22 treatment, the change was not significant. This aligns with previous findings that NRT1.1 phosphorylation affects dynamics and dwell time (Zhang et al., 2019). Additionally, numerous FLS2 exhibited short-lived dwell times, indicating abortive endocytic events associated with the endocytic pathway and signal transduction (Bertot et al., 2018). Therefore, these results underscore the impact of Ser-938 phosphorylation on the spatiotemporal dynamics of flg22-induced FLS2.

Ser-938 phosphorylation enhances recruitment of FLS2/BAK1 heterodimerization into *At*Rem1.3-associated microdomains

Proteins rarely act independently; they typically form multimers to enhance downstream signaling (Li et al., 2022). Previous studies have shown that inactive FLS2 mainly exists as monomers. Flg22 treatment induces FLS2 and BAK1 to heterodimerize at the PM, signifying flg22 as a ligand promoting this heterodimerization (Orosa et al., 2018). Therefore, we further investigated if Ser-938 phosphorylation affects FLS2/BAK1 heterodimerization. Tesseler

segmentation, FRET-FLIM, and smPPI analyses revealed no impact of Ser-938 phosphorylation on FLS2/BAK1 heterodimerization (Figure 2A-C and S2). This aligns with the previous finding that flg22 acts as a molecular glue for FLS2 and BAK1 ectodomains (Sun et al., 2013), confirming the independence of FLS2/BAK1 heterodimerization from phosphorylation, with these events occurring sequentially.

Membrane microdomains serve as pivotal platforms for protein regulation, impacting cellular signaling dynamics (Martinière et al., 2021). Studies reveal that specific plasma membrane (PM) proteins, responsive to developmental cues and environmental stimuli, exhibit dynamic movements within and outside these microdomains (Lee et al., 2019). For instance, treatment with the secreted peptides RAPID ALKALINIZATION FACTOR (RALF1 and RALF23) enhances the presence of FERONIA (FER) in membrane microdomains (Gronnier et al., 2022). Conversely, flg22-activated BSK1 translocates from membrane microdomains to non-membrane microdomains (Su et al., 2021). In a previous investigation, we demonstrated that flg22 induces FLS2 translocation from AtFlot1-negative to AtFlot1-positive nanodomains in the plasma membrane, implying a connection between FLS2 phosphorylation and membrane nanodomain distribution (Cui et al., 2018). To validate this, we assessed the association of FLS2/FLS2^{S938D}/FLS2^{S938A} with membrane microdomains, using *At*Rem1.3-associated microdomains as representatives (Huang et al., 2019). Employing SPT, FRET–FLIM, and Pearson correlation, we found increased correlation coefficients between FLS2-GFP/FLS2^{S938D}-GFP and *At*Rem1.3-mCherry during flg22 treatment compared to the control (Figure 2D-2F and Movies 1-3). Significantly, flg22 treatment did not increase colocalization levels of FLS2^{S938A}-GFP and *At*Rem1.3, indicating the necessity of phosphorylation (Figure 2G-2I). These findings suggest that the phosphorylation state of FLS2 at Ser-938 influences its aggregation into *At*Rem1.3-associated microdomains, providing an efficient

mechanism for triggering the immune response.

Ser-938 phosphorylation maintains FLS2 protein homeostasis via flg22-induced endocytosis

The PM protein endocytosis is crucial for regulating intercellular signal transduction in response to environmental stimuli. Notably, Thr 867 mutation, a potential phosphorylation site on FLS2, results in impaired flg22-induced endocytosis, underscoring the significance of phosphorylation in FLS2 endocytosis (Robatzek et al., 2006). As mentioned earlier, FLS2 phosphomimetic mutants showed a reduced dwell time (Figures 1 H and 1I), implying a probable connection between FLS2 dwell time and endocytosis. Results found that FLS2/FLS2^{S938D}/FLS2^{S938A}-GFP accumulated in BFA compartments labeled with FM4-64, indicating that various Ser-938 phosphorylation states of FLS2 undergo BFA-dependent constitutive endocytosis (Figure 3A, S3A).

Next, we investigated the impact of Ser-938 on flg22-induced FLS2 internalization. Results revealed increased endocytic vesicles for FLS2 during flg22 treatment, aligning with previous studies (Leslie et al., 2017; Loiseau et al., 2017). Employing confocal laser-scanning microscopy (CLSM) during 10μM flg22 treatment, we tracked FLS2 endocytosis and quantified vesicle numbers over time (Figure 3B). It is evident that both FLS2 and FLS2^{S938D} vesicles appeared 15 min after-flg22 treatment, significantly increasing thereafter (Figure 3C). Notably, only a few vesicles were detected in FLS2^{S938A}-GFP, indicating Ser-938 phosphorylation's impact on flg22-induced FLS2 endocytosis. Additionally, fluorescence correlation spectroscopy (FCS) (Chen et al., 2009) monitored molecular density changes at the PM before and after flg22 treatment (Figure S3F). Figure 3D shows that both FLS2-GFP and FLS2^{S938D}-GFP densities significantly decreased after flg22 treatment, while FLS2^{S938A}-GFP exhibited minimal changes, indicating Ser-938 phosphorylation affects FLS2 internalization. Western blotting confirmed that

Ser-938 phosphorylation influences FLS2 degradation after flg22 treatment (Figure 3E), consistent with single-molecule analysis findings. Therefore, our results strongly support the notion that Ser-938 phosphorylation expedited FLS2 internalization, potentially regulating its immune response capacity.

Ser-938 Phosphorylation affects FLS2-mediated responses

PTI plays a pivotal role in host defense against pathogenic infections (Lorrai et al., 2021; Ma et al., 2022). Previous studies demonstrated that FLS2 perception of flg22 initiates a complex signaling network with multiple parallel branches, including calcium burst, mitogen-activated protein kinases (MAPKs) activation, callose deposition, and seedling growth inhibition (Baral et al., 2015; Marcec et al., 2021; Huang et al., 2023). Our focus was to investigate the significance of Ser-938 phosphorylation in flg22-induced plant immunity. Figure 4A-F illustrates diverse immune responses in FLS2 and FLS2^{S938D} plants following flg22 treatment. These responses encompass calcium burst activation, MAPKs cascade reaction, callose deposition, hypocotyl growth inhibition, and activation of immune-responsive genes. In contrast, FLS2^{S938A} (Figure S4A-D) exhibited limited immune responses, underscoring the importance of Ser-938 phosphorylation for FLS2-mediated PTI responses.

In summary, our study confirmed that FLS2 phosphorylation regulated PAMP-triggered plant immunity by influencing spatiotemporal dynamics at the PM (Figure 4 G and H). Following flg22 treatment, activated FLS2 undergoes hetero-oligomerization and phosphorylation sequentially. Crucially, phosphorylation at the Ser-938 site promotes FLS2 recruitment into *At*Rem1.3-associated microdomains and endocytosis. These results provided new insights into the phosphorylation-regulated dynamics of plant immunity, thereby providing a reference for future studies on signal transduction in intracellular complex nanostructures.

Acknowledgments

This work was supported by the National Natural Science Foundation of China (32030010, 91954202, 32370740, 32000483, 32170689), the Fundamental Research Funds for the Central Universities (NO.QNTD202301), National Key Research and Development Program of China (2022YFF0712500, 2022YFD2200603), Beijing Nova Program (20230484251), 5·5 Engineering Research & Innovation Team Project of Beijing Forestry University (BLRC2023C06) and the program of Introducing Talents of Discipline to Universities (111 project, B13007).

Author contributions

J.L., Y.C. and X.L. designed the research; Y.C., H.Q., C.X. and J.Y. performed the research; C.X., P.L. and M.Y. contributed new reagents/analytic tools; X.Z., H.Q. and B.S. analyzed the data; and Y.C., H.Q. and J.L. wrote the paper.

Declaration of interests

The authors declare no competing interests.

Figures and Figure legends

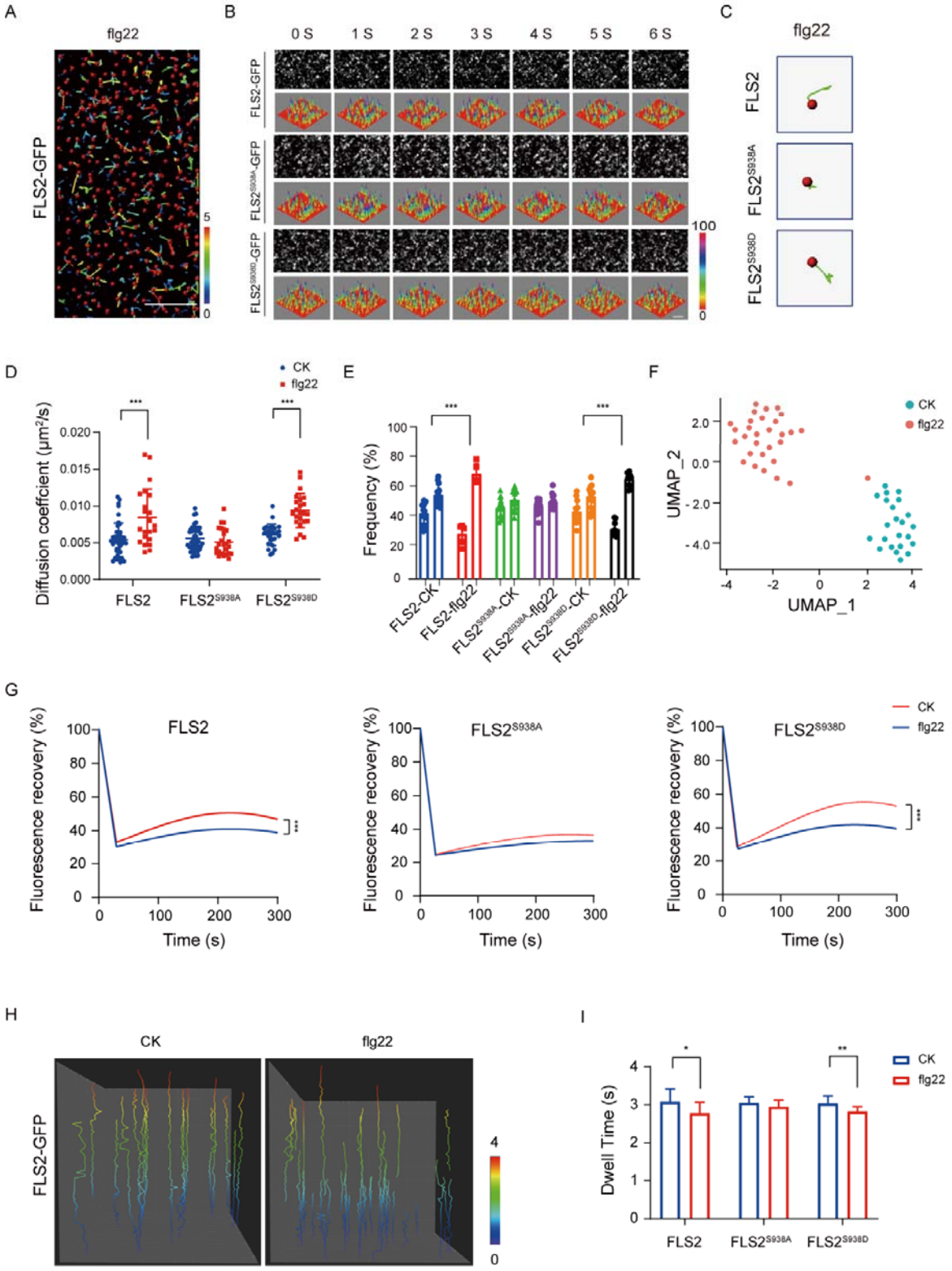

Figure 1. Effects of Ser-938 phosphorylation on the spatiotemporal

dynamics of FLS2 at the plasma membrane.

(A) VA-TIRFM images of a FLS2-expressing hypocotyl cell was analyzed. The 5-day-old transgenic Arabidopsis plant cells were observed under VA-TIRFM. The red balls indicate the positions of the identified points that appeared. Trajectories represent the track length of the identified points. Bar = 10μm. (**B**) Time-lapse images of FLS, $FLS2^{S938A}$, and $FLS2^{S938D}$. Bar = 2 μm. The fluorescence intensity changes among different 3D luminance plots. (**C**) The trajectories of representative individual FLS2, $FLS2^{S938A}$ and $FLS2^{S938D}$ under 30 min for 10 μM flg22 processing. (**D**) Diffusion coefficients of FLS (control, n = 42 spots; flg22, n = 24 spots), $FLS2^{S938A}$ (control, n = 44 spots; flg22, n = 25 spots) and $FLS2^{S938D}$ (control, n = 27 spots; flg22, n = 23 spots) under different environments. Statistical significance was assessed using the Student's *t*-test (***$p < 0.001$). Error bars represent the SD. (**E**) Frequency of long- and short-range motions for FLS, $FLS2^{S938A}$, and $FLS2^{S938D}$ under different environments. Statistical significance assessed with the Student's *t*-test (***$p < 0.001$). Error bars represent the SD. (**F**) UMAP visualization of $FLS2^{S938D}$ samples under different conditions (control, n = 32 spots; flg22, n = 21 spots). Dots represent the individual images, and are colored according to the reaction conditions. (**G**) Fluorescence recovery curves of the photobleached areas with or without the flg22 treatment. Three biological replicates were performed. (**H**) The single-molecule trajectories of FLS2 analyzed by Imaris could be faithfully tracked for 4 s under control and flg22 treatments. (**I**) Dwell times were analyzed for FLS2 (control, n = 18 spots; flg22, n = 16 spots), $FLS2^{S938A}$ (control, n = 19 spots; flg22, n = 24 spots), and $FLS2^{S938D}$ (control, n = 11 spots; flg22, n = 14 spots) under the control and flg22 treatments. Statistical significance assessed with Student's *t*-test (*$p < 0.05$; **$p < 0.01$). Error bars represent the SD.

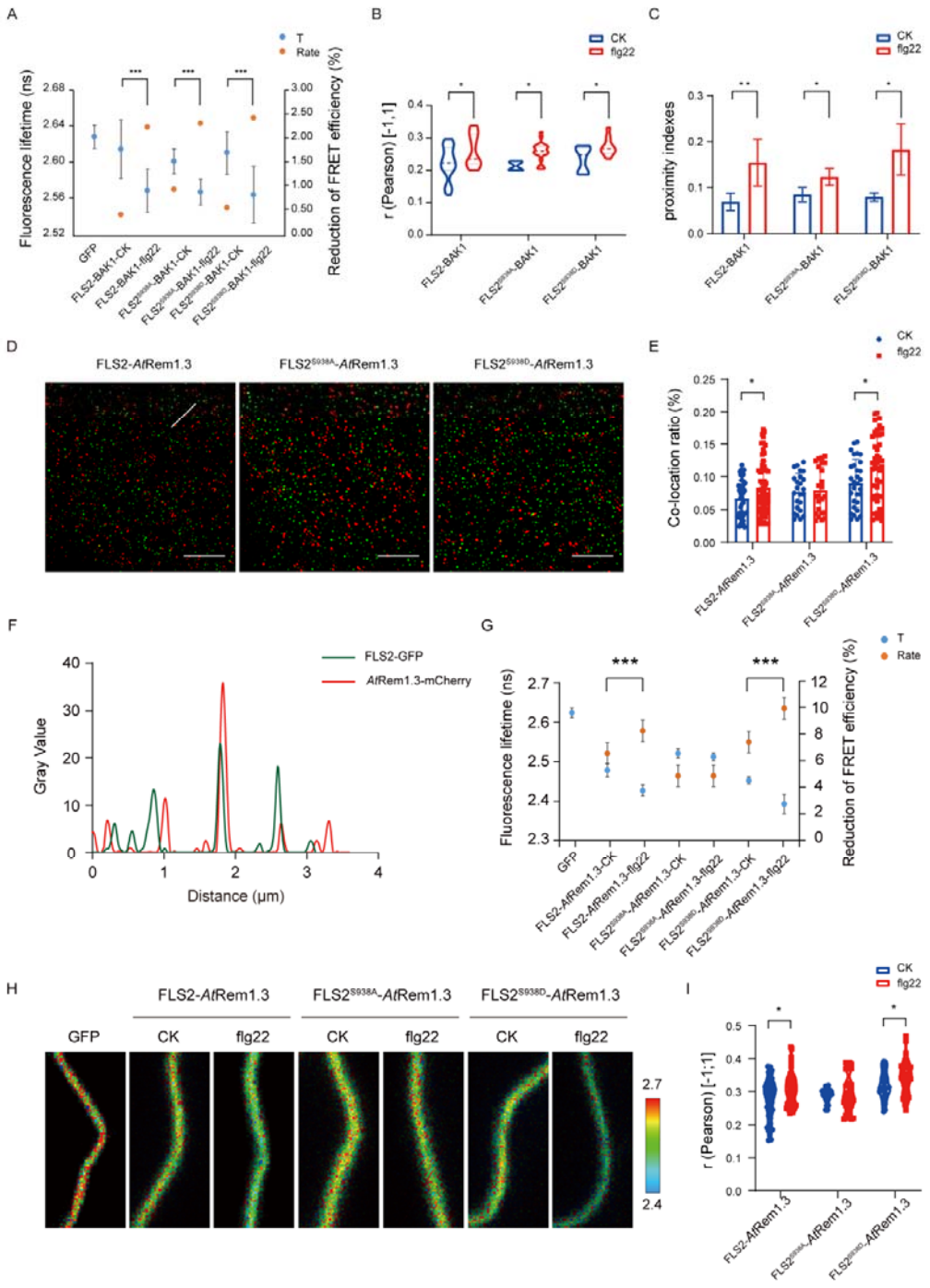

Figure 2. Different Ser-938 phosphorylation states of FLS2 affect its partitioning into *At*Rem1.3-associated microdomains.

(**A**) FLIM-FRET was used to detect the co-expression of FLS2/FLS2^{S938A}/FLS2^{S938D}-GFP and BAK1-mCherry in the *N. benthamiana* epidermal cells stimulated by 1/2 MS or flg22 (10 μM) for 30 min. Average fluorescence lifetime (t) and the FRET efficiency were analyzed for FLS2, FLS2^{S938A} or FLS2^{S938D} and BAK1. Statistical significance was assessed with Student's *t*-test (***$p < 0.001$). Error bars represent the SD. (**B**) Pearson correlation coefficient values of co-localization between FLS2 (control, n = 24 images; flg22 = 15 images), FLS2^{S938A} (control, n = 18 images; flg22 = 22 images), or FLS2^{S938D} (control, n = 15 images; flg22 = 20 images) and BAK1 upon stimulation with control or flg22. Statistical significance was assessed with the Student's *t*-test (*$p < 0.05$). Error bars represent the SD. (**C**) Mean protein proximity indexes showing FLS2 (control, n = 8 images; flg22 = 5 images), FLS2^{S938A} (control, n = 4 images; flg22=3 images) or FLS2^{S938D} (control, n = 4 images; flg22 = 3 images) and BAK1 degree of proximity under different conditions. Statistical significance was assessed with the Student's *t*-test (*$p < 0.05$; **$p < 0.01$). Error bars represent the SD. (**D**) TIRF-SIM images of the Arabidopsis leaf epidermal cells co-expressing FLS2/FLS2^{S938A}/FLS2^{S938D}-GFP and *At*Rem1.3-mCherry. The white line represents the fluorescence signals. Bar = 5 μm. (E) The histogram shows the co-localization ratio of FLS2-GFP (control, n = 52 images; flg22 = 61 images), FLS2^{S938A}-GFP (control, n = 30 images; flg22 = 36 images) or FLS2^{S938D}-GFP (control, n = 34 images; flg22 = 54 images) and *At*Rem1.3-mCherry. Statistical significance assessed with the Student's t-test (*$p < 0.05$). Error bars represent the SD. (**F**) FLS2/FLS2^{S938A}/FLS2^{S938D}-GFP and *At*Rem1.3-mCherry fluorescence signals as shown in D. (**G**) The fluorescence mean lifetime (T) and the corrected fluorescence resonance efficiency (Rate) of FLS2, FLS2^{S938D} or FLS2^{S938A} with co-expressed *At*Rem1.3. Statistical significance was assessed using the Student's *t*-test (***$p < 0.001$). Error bars represent the SD. (**H**) Intensity and lifetime maps of the Arabidopsis leaf epidermal cells co-expressing FLS2/FLS2^{S938A}/FLS2^{S938D}-GFP and *At*Rem1.3-mCherry as

measured by FLIM-FRET. (**I**) Quantification of co-localization between FLS2, FLS2^{S938A} or FLS2^{S938D} and *At*Rem1.3 with and without stimulation with ligands. Pearson correlation coefficient values (*r*) were obtained between FLS2 (control, n = 66 images; flg22 = 53 images) /FLS2^{S938A} (control, n = 42 images; flg22 = 54 images) /FLS2^{S938D}-GFP (control, n = 29 images; flg22 = 38 images) and *At*Rem1.3-mCherry. Statistical significance assessed with the Student's *t*-test (*$p < 0.05$). Error bars represent the SD.

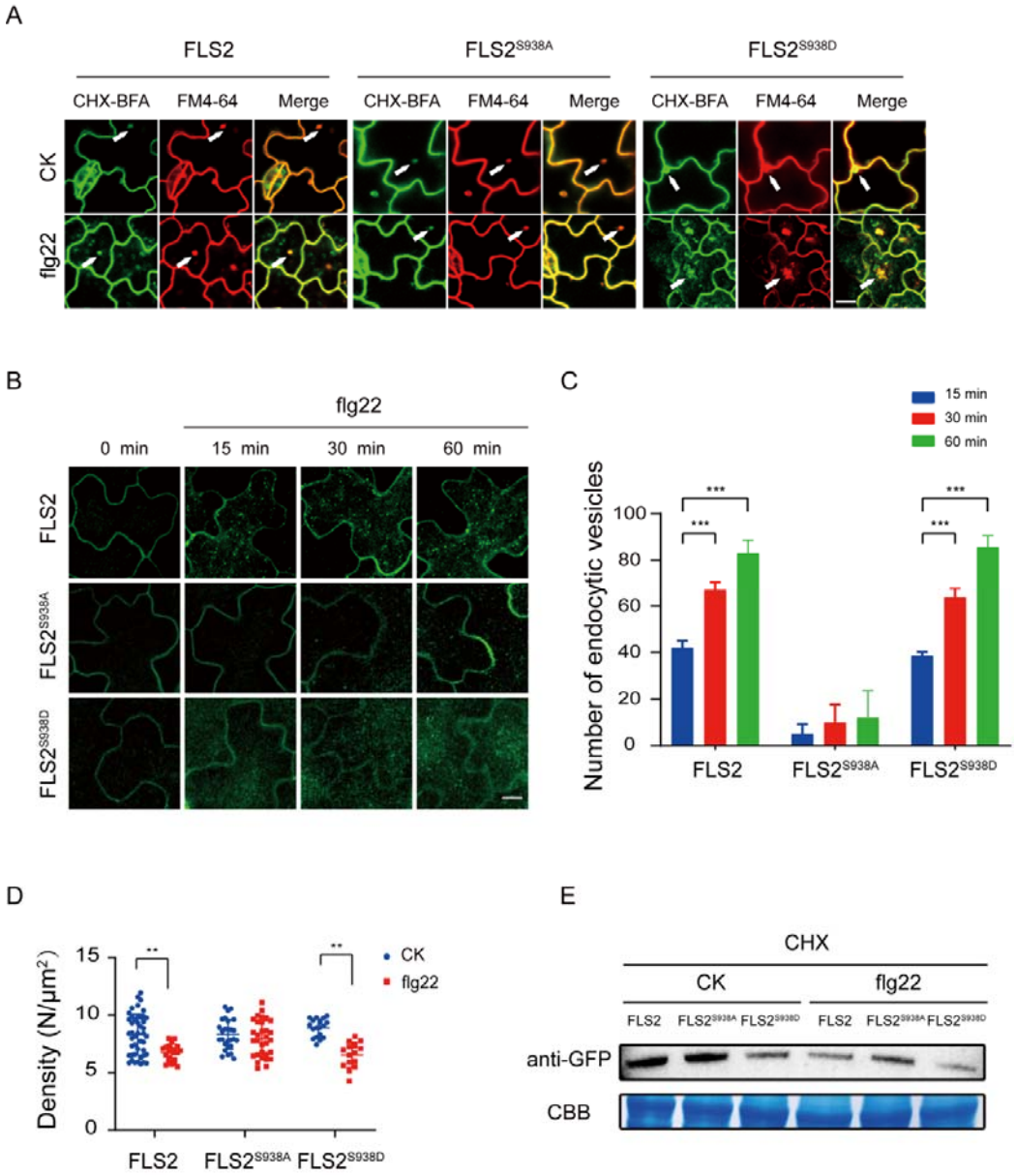

Figure 3. The Ser-938 phosphorylation site affects flg22-induced endocytosis.

(A) Confocal images of FLS2/FLS2^{S938A}/FLS2^{S938D}-GFP in *Arabidopsis thaliana* leaf epidermal cells. The 5-day-old transgenic seedlings were pre-treated with 50 μM CHX for 30 min, then treated with 50 μM BFA for 60 min or CHX + BFA + 5 μM FM4-64 for 30 min, followed by 10 μM flg22 treatment for a total of 30 min. White arrows indicate BFA bodies. Bar = 3μm.

(**B**) Images of FLS2/FLS2^{S938A}/FLS2^{S938D}-GFP in *Arabidopsis thaliana* leaf epidermal cells treated with 10 μM flg22 for 15, 30, and 60 min. Bar = 3μm. (**C**) Analysis of FLS2, FLS2^{S938A}, and FLS2^{S938D} endocytic vesicle numbers in cells treated with 10 μM flg22 treatment over time. Statistical significance assessed using the Student's *t*-test (***$p < 0.001$). Error bars represent the SD. (**D**) The signal density of FLS2, FLS2^{S938A} and FLS2^{S938D} in cells after control or 10 μM flg22 treatments for 30 min as measured by FCS. Statistical significance was assessed using Student's *t*-test (**$p < 0.01$). Error bars represent the SD. (**E**) Immunoblot analysis of FLS2 protein in 10-day-old transgenic Arabidopsis plant upon stimulation with or without 10 μM flg22. CBB, a loading control dyed with Coomassie Brilliant Blue.

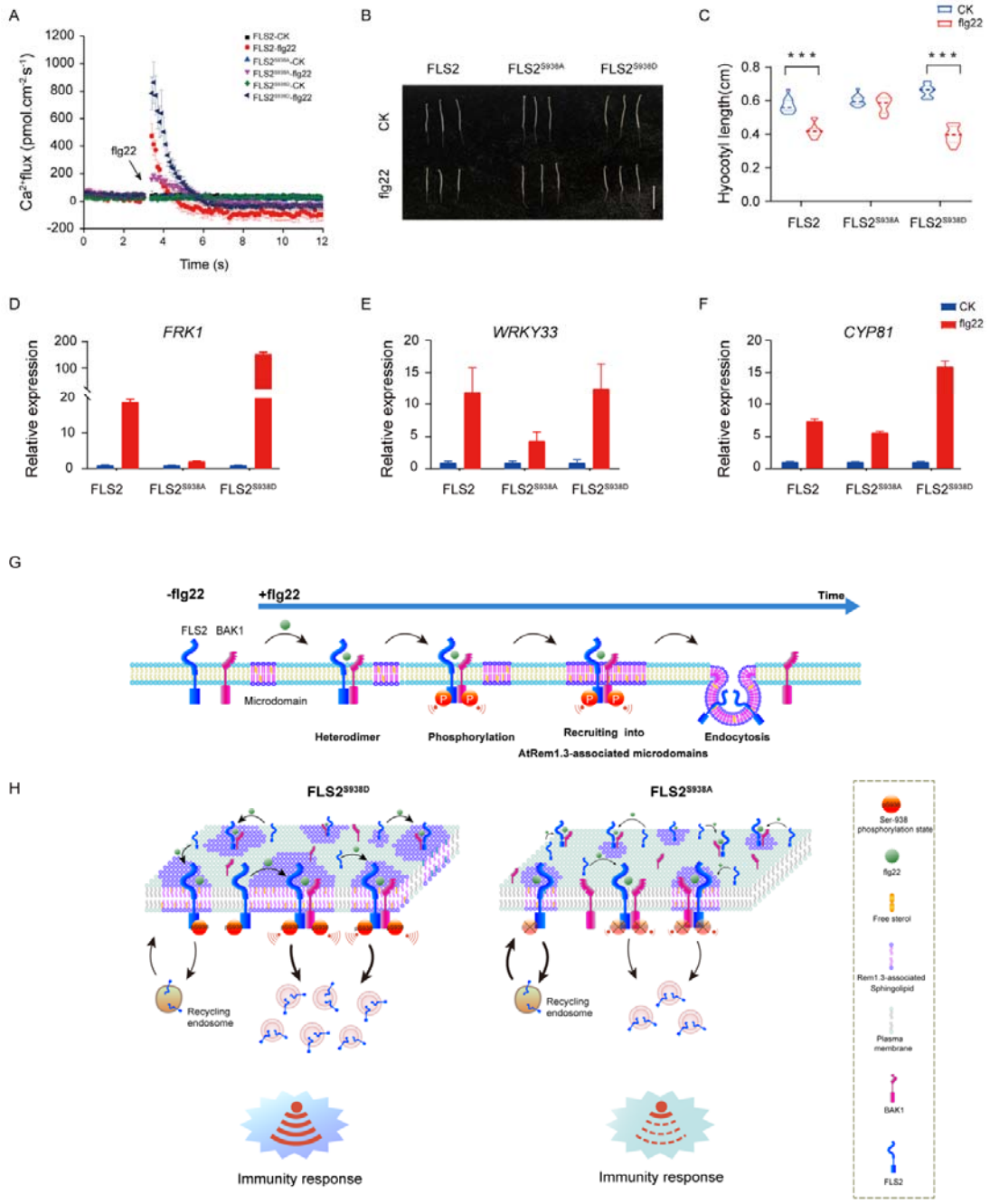

Figure 4. Ser-938 phosphorylation is essential for various flg22-induced PTI responses.

(**A**) The flg22-induced transient Ca^{2+} flux in 20-day-old transgenic leaf cells. The Ca^{2+} flux was continuously recorded for 12 min in the test medium. Each point represents the average value for about 12 individual plants ± SEM (**B**)

Phenotypes of 5-day old etiolated seedlings grown in the presence of 1/2 MS (control) or 10 μM flg22 solid medium. Bar=0.5cm. (**C**) Hypocotyl length of FLS2 (control, n = 13 seedlings; flg22=13 seedlings), FLS2^{S938A} (control, n = 13 seedlings; flg22=13 seedlings) and FLS2^{S938D} (control, n = 13 seedlings; flg22=13 seedlings) transgenic plants. Statistical significance was assessed with the Student's *t*-test (***$p < 0.001$). Error bars represent the SD. (**D-F**) mRNA levels of the PTI marker genes FRK1/WRKY33/CYP81 were significantly different between the FLS2, FLS2^{S938A}, and FLS2^{S938D} 10-day-old transgenic Arabidopsis plant after treatment with 10 μM flg22 for 30 min. Total RNA was extracted from 10-day-old seedlings and analyzed using qRT-PCR, with transcript levels being normalized to *UBQ5*. Error bars represent SD. (**G**) The working model for the spatiotemporal dynamic regulation of FLS2 phosphorylation at the plasma membrane upon flg22 stimulation. (**H**) Dynamic model of FLS2 with different Ser-938 phosphorylation states upon stimulation with flg22.

STAR Methods

Plant Materials and Construction

Mutants and transgenic lines used in all experiments were in the *Arabadopsis thaliana* Colombia-0 (Col-0) background. To generate the transgenic plants, specific constructs were PCR-amplified and cloned into the vector pCAMBIA2300. Plasmids were introduced into the mutant plants by *Agrobacterium*-mediated transformation. Dual-color lines expressing FLS2^{S938A}-GFP and FLS2^{S938D}-GFP with REM1.3-mCherry were generated by hybridization.

Drug Treatments

All chemicals were obtained from Sigma-Aldrich, and dissolved in 100% DMSO to yield stock solutions at the following concentrations: BFA (50 mM in DMSO, 50 μM in working solution), CHX (50 mM in DMSO, 50 μM in working solution), and FM4-64 (5 mM in DMSO, 5 μM in working solution). The flg22 of

flagellin peptides was synthesized by Shanghai GL Biochem Company, and was used in a concentration of 10 μM in double-distilled H2O. *Arabidopsis* seedlings were treated in 1/2 MS growth liquid medium with added hormone or drug.

Quantitative Reverse-transcription PCR

Total RNA was extracted using the Plant Kit (Tiangen), and then reverse transcribed into cDNA with FastQuant RT Kit (Tiangen). Next, qPCR was performed using TiangenSurperRealPreMix Plus (SYBR Geen). The primers used were as follows: WRKY33 (At At2g38470) 5′-GAAACAAATGGTGGGAATGG-3′ and 5′-TGTCGTGTGATGCTCTCTCC-3′; CYP81 (At At2g23190) 5′-AAATGGAGAGAGCAACACAATG-3′ and 5′-ATCGCCCATTCCAATGTTAC-3′; FRK1 (AtAt2g19190) 5′-TATATGGACACCGCGTATAGTG-3′and 5′-ATAAAACTTTGCGTTAGGGTCG-3′.

Aniline Blue Staining

To detect callose deposition, aniline blue staining was performed as described. *Arabidopsis thaliana* leaves were completely de-colored by the destaining solution (3 mL ethyl alcohol and 1 ml glacial acetic acid), rinsed in water and 50% ethanol, and then stained in 150 mM KH_2PO_4 (pH 9.5) plus 0.01% aniline blue for 2 h. Samples were mounted in 25% glycerol, and then observed under a microscope that was equipped with a Leica DM2500 UV lamp.

Confocal Laser Scanning Microscopy and Image Analysis

Confocal microscopy was done with a TCS SP5 Confocal Microscope fitted with a 63X water-immersion objective. GFP and FM4-64 were assayed using 488-nm and 514-nm wavelengths (multitrack mode). The fluorescence emissions were respectively detected with spectral detector set LP 560–640 (FM4-64) and BP 520–555 (GFP). Image analysis was performed with Leica TCS SP5 software and quantified using the ImageJ software bundle (NIH).

VA-TIRFM and Single-Particle Fluorescence Image Analysis

The dynamics of FLS2 phospho-dead and phospho-mimic mutants were recorded using VA-TIRFM. This was done using an inverted microscope (IX-71, Olympus) equipped with a total internal reflective fluorescence illuminator (model no. IX2-RFAEVA-2; Olympus) and a 1003 oil-immersion objective (numerical aperture = 1.45). To track GFP-labeled proteins at the PM, living leaf epidermal cells of 6-day-old seedlings were observed under VA-TIRFM. To visualize GFP or mCherry fluorescent proteins, appropriate corresponding laser excitation (473-nm or 561-nm) was used and emission fluorescence was obtained with filters (BA510IF for GFP; HQ525/50 for mCherry). A digital EMCCD camera (Andor Technology, ANDOR iXon DV8897D-CS0-VP, Belfast, UK) was used to acquire the fluorescent signals, which were stored directly on computers and then analyzed with Image J software. Images of single particles were acquired with 100-ms exposure time.

TIRF-SIM imaging and the colocalization analysis

The SIM images were taken by a 60 × NA 1.49 objective on a structured illumination microscopy (SIM) platform (DeltaVision OMX SR) with a sCMOS camera (Camera pixel size, 6.5 μm). The light source for TIRF-SIM included diode laser at 488 nm and 568 nm with pixel sizes (μm) of 0.0794 and 0.0794 (Barbieri et al., 2021).

For the dual-color imaging, FLS2/FLS2^{S938A}/FLS2^{S938D}-GFP (488 nm/30.0%) and AtRem1.3-mCherry (561 nm/30.0%) were excited sequentially. The exposure time of the camera was set at 50 ms throughout single-particle imaging. The time interval for time-lapse imaging was 100 ms, the total time was 2s, and the total time points were 21s. The Imaris intensity correlation analysis plugin was used to calculate the co-localization ratio.

Ca^{2+} Flux Measurements in Arabidopsis Leaves

Net Ca^{2+} fluxes in Arabidopsis leaf cells were measured using the non-invasive micro-test technique (NMT), as described previously (Zhong et al., 2023). First,

a small incision was made in the leaves of fourteen-day-old seedling. Then it was fixed at the bottom of 35 mm petri dish, and incubated in the test buffer(pH =6.0, 0.1 mmol L^{-1}KCl/$CaCl_2$/$MgCl_2$, 0.2 mmol L^{-1} Na_2SO_4, 0.3 mmol L^{-1} MES, 0.5 mmol L^{-1} NaCl) for approximately 30 min. The Ca^{2+} concentration in the leaf cells was measured at 0.2 Hz near and 30 µm away from the cells. Each plant was measured once, and then use 1/2 MS (CK) or 10 µM flg22 treated the leaf and measured Ca^{2+}flux again. The Ca^{2+} flux was calculated as described (Jiao et al., 2022).

Analysis of Root Growth

Arabidopsis seedlings were treated with different conditions, and imaging was performed by scanning the root systems at 500 dpi (Canon EOS 600D). ImageJ was used to analyze the root growth parameters. Three biological replicates were performed.

FCS

FCS was performed in point-scanning mode on a Leica TCS SP5 FCS microscope equipped with a 488-nm argon laser, an Avalanche photodiode, and an in-house coupled correlator. After acquiring images on the PM of a cell in transmitted light mode, the diffusion of protein molecules into and out of the focal volume transformed the local concentration of fluorophores, leading to spontaneous fluctuation in the fluorescence intensity. Finally, the protein density was calculated on the basis of the protocol described previously.

FRET-FLIM

FRET-FLIM analysis was performed using an inverted Olympus FV1200 microscope equipped with a Picoquant picoHarp300 controller. The excitation at 488 nm was implemented by a picosecond pulsed diode laser at a reduplication rate of 40 MHz, by way of a water immersion objective (603, numerical aperture [NA] 1.2). The emitted light passed through a 520/35 nm bandpass filter and was detected by an MPD SPAD detector. Data were

collected and performed using the SymphoTime 64 software (PicoQuant).

Western Blot

Total proteins were extracted from 10-day-old seedlings of the acidic phosphomimic mutants FLS2^{S938A}-GFP and FLS2^{S938D}-GFP and transgenic FLS2-GFP lines under different conditions. Proteins were extracted using buffer E [includes 1.5125 g Tris-HCl (pH 8.8), 1.2409 g $Na_2S_2O_5$, 11.1 ml glycerine, 1 g SDS, and 5 mM DTT]. The proteins in PM fractions were obtained using the Invent Minute kit. Proteins were separated by 10% SDS-polyacrylamide gel and transferred to a nitrocellulose membrane. The membrane was blotted with anti-GFP antibody (Sigma-Aldrich) at a 1:4000 dilution.

Supplemental data

Supplemental Figure S1. Different Ser-938 phosphorylation states lead to specific spatiotemporal dynamics of FLS2.

Supplemental Figure S2. Different Ser-938 phosphorylation states do not affect the hetero-oligomerization of FLS2/BAK1.

Supplemental Figure S3. Effects of Ser-938 phosphorylation on the endocytosis of FLS2.

Supplemental Figure S4. Ser-938 phosphorylation affects flg22-induced PTI responses.

Supplemental Movies 1-3. TIRF-SIM movies of FLS2 (WT, A, D) and *At*Rem1.3-mCherry.

References

Baral A, Irani NG, Fujimoto M, Nakano A, Mayor S, Mathew MK. 2015. Salt-induced remodeling of spatially restricted clathrin-independent endocytic pathways in Arabidopsis root. *Plant Cell* **27**: 1297-315. DOI: 10.1105/tpc.15.00154. PMID: 25901088

Barbieri L, Colin-York H, Korobchevskaya K, Li D, Wolfson DL, Karedla N, Schneider F, Ahluwalia BS, Seternes T, Dalmo RA, Dustin ML, Li D, Fritzsche M. 2021. Two-dimensional TIRF-SIM-traction force microscopy (2D TIRF-SIM-TFM). *Nature Communications* **12**: 2169. DOI: 10.1038/s41467-021-22377-9. PMID: 33846317

Bertot L, Grassart A, Lagache T, Nardi G, Basquin C, Olivo-Marin J, Sauvonnet N. 2018. Quantitative and statistical study of the dynamics of clathrin-dependent and -independent

endocytosis reveal a differential role of endophilinA2. *Cell Reports* **22**: 1574–1588 doi.org/10.1016/j.celrep.2018.01.039, PMID: 29425511

Boutté Y, Jaillais Y. 2020. Metabolic cellular communications: feedback mechanisms between membrane lipid homeostasis and plant development. *Developmental Cell* **54**: 171–182. DOI: https://doi.org/10.1016/j.devcel.2020.05.005, PMID: 32502395

Bücherl CA, Jarsch IK, Schudoma C, Segonzac C, Mbengue M, Robatzek S, MacLean D, Ott T, Zipfel C. 2017. Plant immune and growth receptors share common signalling components but localize to distinct plasma membrane nanodomains. *eLife* **6**: e25114. DOI: https://doi.org/10.7554/eLife.25114, PMID: 28262094

Cao Y, Aceti DJ, Sabat G, Song J, Makino S, Fox BG, Bent AF. 2013. Mutations in FLS2 Ser-938 dissect signaling activation in FLS2-mediated Arabidopsis immunity. *PLOS Pathogens* **9**: e1003313. DOI: https://doi.org/10.1371/journal.ppat.1003313, PMID: 23637603

Chen Y, Munteanu AC, Huang YF, Phillips J, Zhu Z, Mavros M, Tan W. 2009. Mapping receptor density on live cells by using fluorescence correlation spectroscopy. *Chemistry* **15**: 5327-36. DOI: https://doi.org/10.1002/chem.200802305, PMID: 19360825

Chinchilla D, Bauer Z, Regenass M, Boller T, Felix G. 2006. The Arabidopsis receptor kinase FLS2 binds flg22 and determines the specificity of flagellin perception. *Plant Cell* **18**: 465-476. DOI:10.1105/tpc.105.036574, PMID: 16377758

Cui Y, Li X, Yu M, Li R, Fan L, Zhu Y, Lin J. 2018. Sterols regulate endocytic pathways during flg22-induced defense responses in Arabidopsis. *Development* **145**: dev165688. DOI: https://doi.org/10.1242/dev.165688, PMID: 30228101

Dorrity MW, Saunders LM, Queitsch C, Fields S, Trapnell C. 2020. Dimensionality reduction by UMAP to visualize physical and genetic interactions. *Nature Communications* **11**: 1537. DOI: https://doi.org/10.1038/s41467-020-15351-4, PMID: 32210240

Gada KD, Kawano T, Plant LD, Logothetis DE. 2022. An optogenetic tool to recruit individual PKC isozymes to the cell surface and promote specific phosphorylation of membrane proteins. *Journal of Biological Chemistry* **298**: 101893. DOI: https://doi.org/10.1016/j.jbc.2022.101893, PMID: 35367414

Geng X, Ge B, Liu Y, Wang X, Dong K, Zhang Y, Chen Y, Lu C. 2022. Genome-wide identification and functional analysis of silicon transporter family genes in moso bamboo (*Phyllostachys edulis*). *International Journal of Biological Macromolecules* **223**: 1705–1719. DOI: https://doi.org/10.1016/j.ijbiomac.2022.10.099, PMID: 36252629

Greig J, Bulgakova NA. 2021. Fluorescence recovery after photobleaching to study the dynamics of membrane-bound proteins in vivo using the Drosophila embryo. *Methods in Molecular Biology* **2179**: 145–159. DOI: https://doi.org/10.1007/978-1-0716-0779-4_13, PMID: 32939719

Gronnier J, Franck CM, Stegmann M, DeFalco TA, Abarca A, von Arx M, Dünser K, Lin W, Yang Z, Kleine-Vehn J, Ringli C, Zipfel C. 2022. Regulation of immune receptor kinase plasma membrane nanoscale organization by a plant peptide hormone and its receptors. e*Life* **11**: e74162. DOI: https://doi.org/10.7554/eLife.74162, PMID: 34989334

Huang D, Sun Y, Ma Z, Ke M, Cui Y, Chen Z, Chen C, Ji C, Tran TM, Yang L, Lam SM, Han Y, Shu G, Friml J, Miao Y, Jiang L, Chen X. 2019. Salicylic acid-mediated plasmodesmal closure via Remorin-dependent lipid organization. *Proceedings of the National Academy*

of Sciences of the United States of America **116**: 21274–21284. DOI: https://doi.org/10.1073/pnas.1911892116, PMID: 31575745

Huang Y, Cui J, Li M, Yang R, Hu Y, Yu X, Chen Y, Wu Q, Yao H, Yu G, Guo J, Zhang H, Wu S, Cai Y. 2023. Conservation and divergence of flg22, pep1 and nlp20 in activation of immune response and inhibition of root development. *Plant Science* **331**: 111686. DOI: https://doi.org/10.1016/j.plantsci.2023.111686, PMID: 36963637

Jiao C, Gong J, Guo Z, Li S, Zuo Y, Shen Y. 2022. Linalool activates oxidative and calcium burst and CAM3-ACA8 participates in calcium recovery in Arabidopsis leaves. *International Journal of Molecular Sciences*, **23**: 5357. DOI: https://doi.org/10.3390/ijms23105357, PMID: 35628166

Kim TJ, Lei L, Seong J, Suh JS, Jang YK, Jung SH, Sun J, Kim DH, Wang Y. 2018. Matrix rigidity-dependent regulation of Ca^{2+} at plasma membrane microdomains by FAK visualized by fluorescence resonance energy transfer. *Advanced Science*, **6**: 1801290. DOI: https://doi.org/10.1002/advs.201801290, PMID: 30828523

Kontaxi C, Kim N, Cousin MA. 2023. The phospho-regulated amphiphysin/endophilin interaction is required for synaptic vesicle endocytosis. *Journal of Neurochemistry* **166**: 248–264. DOI: https://doi.org/10.1111/jnc.15848, PMID: 37243578

Lee Y, Phelps C, Huang T, Mostofian B, Wu L, Zhang Y, Tao K, Chang YH, Stork PJ, Gray JW, Zuckerman DM, Nan X. 2019. High-throughput, single-particle tracking reveals nested membrane domains that dictate KRasG12D diffusion and trafficking. *eLife* **8**: e46393. DOI: https://doi.org/10.7554/eLife.46393, PMID: 31674905

Leslie ME, Heese A. 2017. Quantitative analysis of ligand-induced endocytosis of FLAGELLIN-SENSING 2 using automated image segmentation. *Methods in Molecular Biology* **1578**: 39–54. DOI: https://doi.org/10.1007/978-1-4939-6859-6_4, PMID: 28220414

Li B, Meng X, Shan L, He P. 2016a. Transcriptional regulation of pattern-triggered immunity in plants. *Cell Host Microbe* **19**: 641-50. DOI: 10.1016/j.chom.2016.04.011, PMID: 27173932

Li L, Kim P, Yu L, Cai G, Chen S, Alfano JR, Zhou JM. 2016b. Activation-dependent destruction of a co-receptor by a pseudomonas syringae effector dampens plant immunity. *Cell Host Microbe* **20**: 504-514. DOI: https://doi.org/10.1016/j.chom.2016.09.007, PMID: 27736646.b

Li M, Ong CY, Langouët-Astrié CJ, Tan L, Verma A, Yang Y, Zhang X, Shah DK, Schmidt EP, Xu D. 2022. Heparan sulfate-dependent RAGE oligomerization is indispensable for pathophysiological functions of RAGE. *eLife* **11**: e71403. DOI: https://doi.org/10.7554/eLife.71403, PMID: 35137686

Loiseau J, Robatzek S. 2017. Detection and analyses of endocytosis of plant receptor kinases. *Methods in Molecular Biology* **1621**: 177–189. DOI: https://doi.org/10.1007/978-1-4939-7063-6_17, PMID: 28567654

Lorrai R, Ferrari S. 2021. Host cell wall damage during pathogen infection: mechanisms of perception and role in plant-pathogen interactions. *Plants* **10**: 399. DOI: https://doi.org/10.3390/plants10020399, PMID: 33669710

Marcec MJ, Tanaka K. 2021. Crosstalk between calcium and ROS signaling during Flg22-triggered immune Response in Arabidopsis leaves. *Plants* **11**: 14. DOI: 10.3390/plants11010014, PMID: 35009017

Martinière A, Zelazny E. 2021. Membrane nanodomains and transport functions in plant. *Plant Physiology* **187**:1839–1855. DOI: https://doi.org/10.1093/plphys/kiab312, PMID: 35235669

Majhi BB, Sobol G, Gachie S, Sreeramulu S, Sessa G. 2021. BRASSINOSTEROID-SIGNALLING KINASES 7 and 8 associate with the FLS2 immune receptor and are required for flg22-induced PTI responses. *Molecular Plant Pathology* **22**: 786-799. DOI: https://doi.org/10.1111/mpp.13062, PMID: 33955635

Mitra SK, Chen R, Dhandaydham M, Wang X, Blackburn RK, Kota U, Goshe MB, Schwartz D, Huber SC, Clouse SD. 2015. An autophosphorylation site database for leucine-rich repeat receptor-like kinases in *Arabidopsis thaliana*. *The Plant Journal* **82**: 1042–1060. DOI: https://doi.org/10.1111/tpj.12863, PMID: 25912465

Offringa R, Huang F. 2013. Phosphorylation-dependent trafficking of plasma membrane proteins in animal and plant cells. *Journal of Integrative Plant Biology* **55**: 789–808. DOI: https://doi.org/10.1111/jipb.12096, PMID: 23945267

Orosa B, Yates G, Verma V, Srivastava AK, Srivastava M, Campanaro A, De Vega D, Fernandes A, Zhang C, Lee J, Bennett MJ, Sadanandom A. 2018. SUMO conjugation to the pattern recognition receptor FLS2 triggers intracellular signalling in plant innate immunity. *Nature Communications* **9**: 5185. DOI: https://doi.org/10.1038/s41467-018-07696-8, PMID: 30518761

Palladino END, Bernas T, Green CD, Weigel C, Singh SK, Senkal CE, Martello A, Kennelly JP, Bieberich E, Tontonoz P, Ford DA, Milstien S, Eden ER, Spiegel S. 2022. Sphingosine kinases regulate ER contacts with late endocytic organelles and cholesterol trafficking. *Proceedings of the National Academy of Sciences of the United States of America* **119**: e2204396119. DOI: https://doi.org/10.1073/pnas.2204396119, PMID: 36122218

Robatzek S, Chinchilla D, Boller T. 2006. Ligand-induced endocytosis of the pattern recognition receptor FLS2 in Arabidopsis. *Genes Development* **20**: 537–542. DOI: https://doi.org/10.1101/gad.366506, PMID: 16510871

Su B, Zhang X, Li L, Abbas S, Yu M, Cui Y, Baluška F, Hwang I, Shan X, Lin J. 2021. Dynamic spatial reorganization of BSK1 complexes in the plasma membrane underpins signal-specific activation for growth and immunity. *Molecular Plant* **14**: 588–603. DOI: https://doi.org/10.1016/j.molp.2021.01.019, PMID: 33524551

Sun Y, Li L, Macho AP, Han Z, Hu Z, Zipfel C, Zhou JM, Chai J. 2013. Structural basis for flg22-induced activation of the Arabidopsis FLS2-BAK1 immune complex. *Science* **342**: 624-628. DOI: https://doi.org/10.1126/science.1243825, PMID: 24114786

Vitrac H, Mallampalli VKPS, Dowhan W. 2019. Importance of phosphorylation/dephosphorylation cycles on lipid-dependent modulation of membrane protein topology by posttranslational phosphorylation. *Journal of Biological Chemistry* **294**: 18853–18862. DOI: https://doi.org/10.1074/jbc.RA119.010785, PMID: 31645436

Xue Y, Xing J, Wan Y, Lv X, Fan L, Zhang Y, Song K, Wang L, Wang X, Deng X, Baluška F, Christie JM, Lin J. 2018. Arabidopsis blue light receptor phototropin 1 undergoes blue light-induced activation in membrane microdomains. *Molecular Plant* **11**: 846-859. DOI: 10.1016/j.molp.2018.04.003, PMID: 29689384

Xing J, Ji D, Duan Z, Chen T, Luo X. 2022. Spatiotemporal dynamics of FERONIA reveal alternative endocytic pathways in response to flg22 elicitor stimuli. *New Phytologist* **235**:

518-532. DOI: 10.1111/nph.18127, PMID: 35358335

Yu X, Xie Y, Luo D, Liu H, de Oliveira MVV, Qi P, Kim SI, Ortiz-Morea FA, Liu J, Chen Y, Chen S, Rodrigues B, Li B, Xue S, He P, Shan L. 2023. A phospho-switch constrains BTL2-mediated phytocytokine signaling in plant immunity. *Cell* **186**: 2329-2344.e20. DOI: https://doi.org/10.1016/j.cell.2023.04.027, PMID: 37192618

Zhai K, Liang D, Li H, Jiao F, Yan B, Liu J, Lei Z, Huang L, Gong X, Wang X, Miao J, Wang Y, Liu JY, Zhang L, Wang E, Deng Y, Wen CK, Guo H, Han B, He Z. 2021. NLRs guard metabolism to coordinate pattern- and effector-triggered immunity. *Nature* **601**: 245-251. DOI: https://doi.org/10.1038/s41586-021-04219-2, PMID: 34912119

Zhang X, Cui Y, Yu M, Su B, Gong W, Baluška F, Komis G, Šamaj J, Shan X, Lin J. 2019. Phosphorylation-mediated dynamics of nitrate transceptor NRT1.1 regulate auxin flux and nitrate signaling in lateral root growth. *Plant Physiology* **181**: 480–498. DOI: https://doi.org/10.1104/pp.19.00346, PMID: 31431511

Zhong YH, Guo ZJ, Wei MY, Wang JC, Song SW, Chi BJ, Zhang YC, Liu JW, Li J, Zhu XY, Tang HC, Song LY, Xu CQ, Zheng HL. 2023. Hydrogen sulfide upregulates the alternative respiratory pathway in mangrove plant *Avicennia marina* to attenuate waterlogging-induced oxidative stress and mitochondrial damage in a calcium-dependent manner. *Plant Cell and Environment* **46**: 1521-1539. DOI: https://doi.org/10.1111/pce.14546, PMID: 36658747

Zhou R, Liu H, Ju T, Dixit R. 2020. Quantifying the polymerization dynamics of plant cortical microtubules using kymograph analysis. *Methods in Cell Biology* **160**: 281–293. DOI: https://doi.org/10.1016/bs.mcb.2020.04.006, PMID: 3289